Carbon Nanosphere-Encapsulated Fe Core-Shell Structures for Catalytic CO_2 Hydrogenation

Daniel Weber[1,a], Ning Rui[2,a], Feng Zhang[2], Heng Zhang[3], Dimitriy Vovchok[2], Michael Wildy[4], Kevin Arizapana[4], Alexa Saporita[1], Jin Zhong Zhang[3,*], Sanjaya D. Senanayake[2], Ping Lu[4,*] and Cheng Zhang[1,*]

[1] Chemistry Department, Long Island University (Post), Brookville, NY 11548, USA; emails: Daniel.weber4@my.liu.edu (D.W.); alexa.saporita@my.liu.edu (A.S.)

[2] Chemistry Division, Brookhaven National Laboratory, Upton, NY 11973, USA; email: ruining@bnl.gov (N.R.); fzhang@bnl.gov (F.Z.); dvovchok@bnl.gov (D.V.); ssenanay@bnl.gov (S.S.)

[3] Department of Chemistry and Biochemistry, University of California, Santa Cruz, CA 95064, USA; emails: hzhan290@ucsc.edu (H.Z.)

[4] Department of Chemistry and Biochemistry, Rowan University, Glassboro, NJ 08028, USA; email: wildym28@rowan.edu (M.W.); arizap27@students.rowan.edu (K.A.)

[a] Authors contributed equally

* Correspondence: emails: cheng.zhang@liu.edu (C.Z.); Tel.: 01-516-299-2013; Fax: 01-516-299-3944; lup@rowan.edu (P.L.); Tel: 01-856-256-5463; zhang@ucsc.edu (J.Z.Z.); Tel: 01-831-459-3776.

Abstract: We synthesized a unique carbon nanosphere (CNS)-encapsulated Fe core-shell catalyst (CNS-Fe) for CO_2 hydrogenation. The synthesized CNS-Fe catalyst exhibited a core-shell structure with the core at ca. 40 nm containing iron species and shell thickness at ca. 10 nm composed of mainly graphitic carbon. X-ray diffraction (XRD), x-ray photoelectron spectroscopy (XPS), Raman spectroscopy and thermogravimetric analysis (TGA) were used to characterize the fresh and spent CNS-Fe catalysts and reveal a mixture of Fe_3O_4, metallic Fe and Fe_5C_2 in the core and graphitic carbon as the shell with defect sites. Hydrogen temperature programmed reduction (H_2-TPR), x-ray absorption near edge structure (XANES) and extended x-ray absorption fine structure (EXAFS) for the fresh CNS-Fe confirmed the composition of the iron species encapsulated in the CNS. The catalytic performance of CNS-Fe was investigated at ambient pressure for CO_2 hydrogenation with hydrocarbons (CH_4, C_2-$C_4^=$, C_2-C_4^0) observed and CO as the main product.

Keywords: CO_2 hydrogenation, carbon nanosphere encapsulated iron, core-shell structure, light olefins, nano-reactor

1. Introduction

Carbon-rich fossil fuels like petroleum, coal and natural gas have been powering human civilization, however, the vast emission of CO_2 as a greenhouse gas has caused severe environmental issues.[1] There is an urgent need to control CO_2 emission to alleviate its negative impact on the environment. In recent years, carbon capture and utilization have been receiving progressively more attention worldwide.[2-4] Transforming CO_2 into value-added fuels and chemicals has become an urgent task to reduce greenhouse gas emission and achieve carbon recycling.[5,6]

Catalytic conversion of CO_2 into value-added products holds promise to alleviate CO_2 emissions.[7-11] Value-added products such as CO and CH_4, light olefins (C_2-$C_4^=$), light alkanes (C_2-C_4^0) and C_{5+} hydrocarbons have important applications in household and industrial processes. Among the hydrocarbons, light olefins such as ethylene, propylene and butylene ($C_2^=$-$C_4^=$) are the building blocks for a wide variety of applications in packaging materials, polymers, plastics, solvents, and cosmetics.[5,12,13] One primary pathway to produce hydrocarbons from CO_2 reduction by hydrogen (H_2) is CO_2−Fischer−Tropsch (CO_2−FTS) route, which consists of two consecutive processes, the reverse water-gas shift (RWGS) reaction (Eqn. 1) and subsequent Fischer−Tropsch synthesis (FTS) (Eqn. 2) as listed below. Fe-based catalysts are widely investigated for CO_2-FTS route due to their moderately high activity for reactions invoving RWGS and FTS. The thermodynamic values in equations (Eqns. 1-4) indicate that lower temperatures favor FTS (Eqns. 2-4), while higher temperatures are needed to activate CO_2 (Eqn. 1) for fast reaction rates.[14] The complex reaction network and thermodynamics suggest that design and synthesis of catalysts for a one-step process to selectively produce desired products is challenging.

The CO_2 hydrogenation related reactions are listed as follow:

CO_2-FTS reaction pathway:

Reverse water-gas shift reaction (RWGS):

$$CO_2 + H_2 \rightarrow CO + H_2O \qquad \Delta H_0^{298} = 41.1\ kJmol^{-1} \qquad (1)$$

Fischer-Tropsch synthesis to olefins (FTS):

$$nCO + 2nH_2 \rightarrow (CH_2)_n + nH_2O \qquad \Delta H_0^{298} = -210.2\ kJmol^{-1}\ (n=2) \qquad (2)$$

Olefin hydrogenation:

$$(CH_2)_n + H_2 \rightarrow C_nH_{2n+2} \qquad \Delta H_0^{298} = -136.3\ kJmol^{-1}\ (n=2) \qquad (3)$$

CO_2 methanation

$$CO_2 + 4H_2 \rightarrow CH_4 + 2H_2O \qquad \Delta H_0^{298} = -165.0\ kJmol^{-1} \qquad (4)$$

Various transition metals in metallic form or metal carbide in bulk and supported forms have been intensively investigated for CO_2 conversion.[12,15-24] It remains a main research objective to improve catalyst performance by preparing small metal particles that are stable under reaction conditions. Confined nano-catalysts based on the unique concept of a nano-reactor have received increasing attention in recent years.[25-38] Previous studies have shown that metal or metal oxide nanoparticles inside carbon nanotubes (CNT) exhibited stronger catalytic activities than metal deposited on the outside walls of CNT due to the

effects of electronic properties and spatial confinement on catalytic activities.[25,26] Metal nanoparticles in the nano-channels of CNTs are also less likely to oxidation.[39,40] Furthermore, the CNT channels can help to reduce aggregation of nanoparticles.[40] On the other hand, the long diffusion length for the reactants and the products to diffuse through the long inner channel of CNTs in which the active catalysts are located during catalysis causes consecutive reactions to take place, making it difficult to limit undesired side reactions such as olefin hydrogenation, olefin oligomerization and even coke formation.

To address issues resulting from higher aspect ratios of CNT, several studies have been reported on the synthesis and applications of core-shell nanocatalysts.[25,26,29,41-47] Gupta *et al* synthesized a core-shell nanocatalyst with optimal amount of Fe_3O_4 and Fe_5C_2 in the core and partially graphitized carbon in the shell for efficient CO_2 hydrogenation.[48] Fe_3O_4 nanoparticles encapsulated inside graphitic carbon shells (Fe_3O_4@carbon) have been found to be more efficient than conventional catalysts.[49,50] Porous graphene-confined Fe-K was found to be a highly efficient catalyst for direct CO_2 hydrogenation to light olefins.[51] Carbon-confined magnesium hydride nano-lamellae was designed for catalytic hydrogenation of CO_2 to light olefins.[4] It was reported that the Fe_3O_4 was responsible for RWGS converting CO_2 to CO (Eqn. 1), the metallic Fe and iron carbides could activate CO to produce hydrocarbons (Eqn. 2).[52,53] Fe_3O_4@carbon nanostructured catalyst affords the advantage of efficient diffusion of carbon atoms from the shell into the core to form Fe_5C_2 carbide phase that is active for hydrogenation.[48,49] Several chemical routes have been developed for the synthesis of Fe_3O_4@carbon nanostructures.[48,49,54,55]

In this work, we synthesized carbon nanospheres (CNS) encapsulated Fe catalysts using an iron polymeric complex (IPC) as a template and dispersant during the resorcinol (R)-formaldehyde (F) polymerization process, followed by carbonization. Our earlier efforts on the synthesis of CNS by adjusting the polymerization temperature, polymerization duration, carbonization temperature and mole ratio of iron content to resorcinol have established the optimized approach to the synthesis of CNS as specified in the experimental section. The fresh catalyst was characterized by scanning electron microscopy (SEM), transmission electron microscopy (TEM), hydrogen temperature programmed reduction (H_2-TPR) and extended x-ray absorption fine structure (EXAFS) to confirm the composition of the iron species encapsulated in the CNS. The catalytic performance of CNS-Fe was investigated at ambient pressure for CO_2 hydrogenation and hydrocarbons (CH_4, C_2-$C_4^=$, C_2-C_4^0) were produced, together with CO as the main by-product. X-ray diffraction (XRD), x-ray photoelectron spectroscopy (XPS), Raman spectroscopy and thermogravimetric analysis (TGA) were used to characterize the fresh and spent CNS-Fe catalysts, and revealed a mixture of Fe_3O_4, metallic Fe and Fe_5C_2 in the core and graphitic carbon with defect sites in the shell.

2. Materials and Methods

2.1 Materials

Iron powder (200 mesh) was purchased from Alfa Aesar. Ammonium hydroxide (28% in water), resorcinol and formaldehyde (37% in water) were purchased from Sigma-Aldrich. Citric acid were purchased from Acros Organics. All chemicals were used without further treatment.

2.2 Synthesis of CNS-Fe

The synthesis of CNS encapsulated Fe catalyst was modified based on our previously reported method.[41,56-59] The procedure was composed of three steps: 1) *synthesis of iron polymeric complex (IPC) solution (0.20 M)*: 19.21 g of citric acid and 5.56 g of iron powder in 1:1 molar ratio, and 100 ml of de-ionized water were placed in a 500 ml beaker. The above mixture was vigorously stirred in an open air for 48 hours, resulted in a clear greenish-yellow solution which was filtered for further use. *2) polymerization process*: in a round-bottom three-neck flask, 12.20 g of resorcinol, 18.0 g of formaldehyde (37% in water) and 100 ml of 0.2M IPC solution were added. The resulted mixture was stirred until resorcinol was completely dissolved. To the above solution, ammonium hydroxide (28% in water) was added dropwise with strong mechanical agitating until the pH reached to 10. The formed slurry was then cured at 85 °C for three hours. The solid (polymer) was collected by filtration and dried at 65 °C in an oven overnight. 3) *carbonization process*: under the nitrogen flow, the collected polymer was heated at 85°C for two hours, followed by heating to 850 °C at 20°C /min and hold at 850 °C for 5 hours. The sample from this step was labeled as CNS-Fe. CNS-Fe with varying Fe contents were prepared using similar manner by changing the molar ratio of resorcinol to iron in IPC (1:1 and 1:3).

2.3 Catalyst Evaluation

The synthesized catalyst was evaluated using a quartz tube (4 mm i.d., 6.35 mm o.d.) flow bed reactor at varying temperatures and ambient pressure. For each catalyst testing, approximately 100 mg of catalyst with uniform mesh size of 40−60 was loaded into the quartz tube with two pieces of quartz wool fixed on both sides of the catalyst. The catalyst was reduced in a 50% H_2/N_2 stream (40 mL min^{-1} in total) at 450°C for 2 hours, and then cool down to 275 °C prior to CO_2 hydrogenation. If not specifically for varying CO_2/H_2 volume ratio, the feed gas, CO_2, H_2, and N_2, with a 1/3/1 ratio (40 mL min^{-1} in total) was introduced into the reactor at atmospheric pressure. The catalyst was then ramped from 275 °C to 400 °C at 25~50 °C increments. The product stream was analyzed on-line using a gas chromatography (GC, Agilent 8890), equipped with a flame ionization detector (FID) and a thermal conductive detector (TCD). HP-PLOT Q capillary column was attached to FID for the separation and quantification of hydrocarbons. The Mol Sieve 5Å PLOT capillary column was attached to TCD for detection of N_2, H_2, CO_2, CO and CH_4. Sequence run was arranged in a queue to collect data at different temperatures. At each temperature, six GC data points were collected. The reaction parameters such as CO_2 conversion (Eqn. 5), hydrocarbon (CH_4, C_2-$C_4^=$, C_2-C_4^0, C_{5+}) (Eqn. 6), CO selectivity (Eqn. 7) and iron time yield (FTY) (Eqn. 8) are defined as:

$$CO_2 \text{ Conversion} = \frac{\mathbf{n}_{\mathbf{CO_2}\,(\mathbf{in})} - \mathbf{n}_{\mathbf{CO_2}\,(\mathbf{out})}}{\mathbf{n}_{\mathbf{CO_2}\,(\mathbf{in})}} \times 100 \quad (5)$$

$$\text{Hydrocarbon distribution} = \frac{n_{\text{product i}}\,(\text{out}) \times \text{carbon number}}{\sum n_i\,(\text{out}) \times \text{carbon number} - n_{CO}(\text{out})} \times 100 \quad (6)$$

$$\text{CO Selectivity} = \frac{n_{CO}(\text{out}) \times \text{carbon number}}{\sum n_i\,(\text{out}) \times \text{carbon number}} \times 100 \quad (7)$$

$$\text{FTY} = \frac{CO_2 \text{ converted in } \mu\text{mol}}{[\text{g of iron content in the catalyst}] \cdot [\text{time in second}]} \quad (8)$$

where n_{CO_2}(in) and n_{CO_2}(out) are the number of moles of CO_2 fed and not converted, respectively. $n_{\text{product i}}$ refers to the mole of the product i; carbon number refers to the number of carbons contained in the product i; $\sum n_i\ (\text{out})$ refers to the total number of moles of the carbon-containing products produced in the reaction.

2.4 Catalyst Characterization

Fe content in CNS were determined by ICP-MS (Agilent 7900 ICP-MS). The samples were first acid extracted using concentrated HNO_3 (67 - 70%, VWR ARISTAR PLUS for trace metal analysis) under intermittent sonication for 24 h, followed by filtration to remove carbon particles using 0.45 μm syringe filter, and the clear filtrate was diluted to estimated final concentrations in a range of 1 – 200 ppb using 1% HNO_3 aqueous solution. Eight standard solutions containing 0, 1, 5, 10, 30, 50, 100 and 200 ppb Fe were used to construct a standard calibration curve for calculating the exact Fe concentration in sample solutions. ICP-grade HNO_3 (metal contents < 1 ppb) and HPLC-grade water (18.2 MΩ·cm, filtered by 0.22 μm membrane filter) were used to prepare the sample and standard solutions.

Powder X-ray diffraction (XRD) patterns were collected on a Bruker D8 Discover Diffractometer using CuKa radiation (40 kV and 40 mA) with degrees per step and time/step parameters of 0.02 degrees per step and0.5 s/step, respectively at 2 theta angle from 10 to 70°. X-ray diffraction patterns were plotted in Origin and processed using the GSAS II software 34 to obtain structural information via Rietveld refinement. Thermogravimetric analysis (TGA) was performed using a TA Q600 thermal analyzer. In a typical measurement, around 10 mg of catalysts were heated in an alumina pan from room temperature (~20 °C) to 650 °C at 10 °C/min ramp rate with 100 ml/min dry nitrogen purging rate.

H_2 temperature-programmed reduction (H_2-TPR) was performed on a Micromeritics Au-to Chem 2920II instrument. Typically, the sample loaded (~50 mg) in a quartz reactor was first pretreated with high-purity He at 350 °C for 1 h. After the sample was cooled down to 35 °C, H_2-TPR was performed in 10% vol H_2 flow by raising the temperature to 750 °C at a rate of 10 °C min^{-1}. A TCD detector was used to monitor the consumption of H_2.

X-ray Photoelectron Spectroscopy (XPS) measurements were carried out using a SPECS AP-XPS chamber at Brookhaven National Laboratory (BNL). It was equipped with a PHOIBOS 150 EP MCD-9 as analyzer and Al Kα (h_V=1486.6 eV) radiation as X-ray source. Powder sample was pressed into a plate made of aluminum and sujected into an ultrahigh-vacuum atmosphere, where a Al X-ray source was used

as the excitation source to probe the material. The XPS spectra were performed with an emission current of 20 mA and the anode potential of 15 kV.

Raman analysis was performed using a Thermo Fisher DRX3 Raman Micro Spectrometer. The laser excitation source was a diode laser (λex = 785 nm). Spectra were recorded under the following conditions: stainless steel substrate, 50x objective, collect exposure time 30s for 8 accumulations, laser power 1.5 mW (in focus) and aperture 50 μm slit. Raman spectra were recorded from ~5 different sample spots, depending on the homogeneity of the sample.

Ex situ Fe K-edge extended X-ray absorption fine structure (EXAFS) and x-ray absorption near edge structure (XANES) measurements were carried out at beamlines 8- ID (ISS) at NSLS-II in fluorescence detection mode. Athena software was used to process all X-ray absorption data.[60]

The samples for Transmission Electron Microscopy (TEM) were prepared as described previously.[41]

3. Results and Discussion

3.1 Role of Iron Precursor IPC in the Synthesis of CNS-Fe

As shown in Scheme 1, the CNS-Fe was synthesized using an iron precursor, iron polymeric complex (IPC), as a template and dispersant during the resorcinol (R)-formaldehyde (F) polymerization process, followed by carbonization. The current preparation method differs from our early works [41,56-59] by skipping the acid/oxidant treatment so that the iron was retained in the core of the core-shell structure. During the synthesis of CNS-Fe, the IPC played a key role as a dispersing agent in the polymerization process.[41] The unique porous structure of IPC assisted the dispersion and stabilization of the resorcinol-formaldehyde gel which led to the formation of the uniform carbon precursor (RF–$Fe(OH)_3$) after the addition of ammonium hydroxide. The obtained iron source in RF–$Fe(OH)_3$ served as both a template and catalyst precursor in the carbonization process by forming carbon nanosphere encapsulated iron core–shell structure (CNS-Fe).

The Fe species is encapsulated in the core of CNS in the synthesis. During the polymerization process, varying amounts of iron precursor (IPC) with mole ratios of Fe/Resorcinol =1/3, 2/3, and 3/3 were employed for the synthesis of CNS-Fe, and the Fe contents in the CNS was determined to be 7.2 wt%, 16.3 wt% and 16.4 wt%, respectively. The results indicated that the Fe content in the CNS reached a saturation point at ca. 16 wt%. The CNS-Fe (7.2 wt%) was the main catalyst tested and characterized in this work. CNS-Fe with other metal contents (16.3% and 16.4 wt%) were only used when specified.

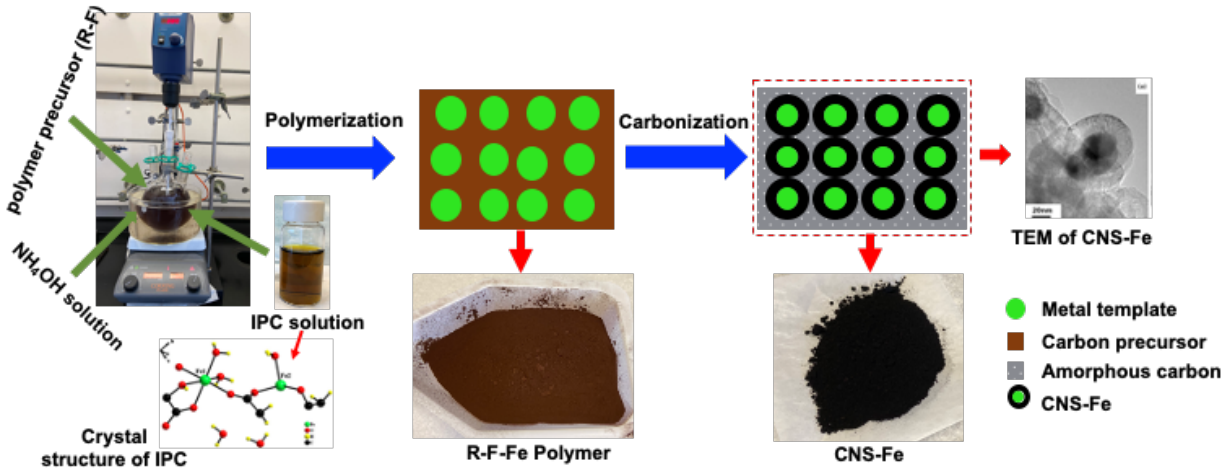

Scheme 1. Synthetic procedures for the preparation of CNS encapsulated iron core-shell structure (CNS-Fe).

The synthesized fresh CNS-Fe was characterized by TEM, XRD, XPS, TGA, H_2-TPR, Raman, XANES and EXAFS to determine the morphologies and detailed structures of the CNS encapsulated iron core-shell architecture. The synthesized CNS-Fe was evaluated for the CO_2 hydrogenation reaction using a flow-bed reactor under different temperatures at ambient pressure with on-line GC analysis. The CNS-Fe after the catalysis testing (spent catalyst) was compared to the fresh CNS-Fe in XRD, XPS, TGA and Raman studies.

3.2 Physicochemical Properties of Fresh CNS-Fe

The morphologies of the synthesized materials were determined in our earlier work as spherical carbon nanostructures with average inner diameter of CNS at ca. 50 nm and particle size distribution of ca. 40 nm.[41,56] The TEM image as shown in Figure 1a clearly shows the core-shell structure with the core at ca. 40 nm as iron species and shell thickness at ca. 10 nm as graphitic carbon with some defect sites. The detailed graphitic layers are shown in Figure 1b.

The CNS encapsulated iron core-shell catalyst was characterized by hydrogen temperature programmed reduction (H_2-TPR) to investigate the reducibility of the active site. As shown in Figure 1c, one main reduction peak centered at ca. 500 °C corresponding to the reduction of $Fe_2O_3 \rightarrow Fe_3O_4$. Further reduction of $Fe_3O_4 \rightarrow \alpha$-Fe occurred at ca. 650 °C with a long tail on the high-temperature side and became more intense in comparison to the supported catalysts.[25] The $Fe_3O_4 \rightarrow \alpha$-Fe reduction peak occurred at ca. 600 °C for supported catalysts.[61,62] The observed 50°C shift was probably due to the restricted diffusion of H_2 through the carbon shell, causing the reduction to occur at higher temperatures. The small H_2 consumption peaks before 400 °C may be attributed to the hydrogenation of functional groups on the surface of the carbon shell, such as hydroxyl and C=O groups.[49]

The ex-situ x-ray absorption spectra were obtained to identify the valence state of iron. XANES and EXAFS measurements for the fresh CNS-Fe were performed and compared with Fe_3O_4, Fe_2O_3, FeO, and

Fe foil as references. As shown in Figure 1d-e, the iron species in CNS-Fe is similar to both Fe_3O_4 and Fe_2O_3, indicating the iron species in the core of CNS contains Fe_3O_4 and Fe_2O_3. Based on the XANES spectra in Figure 1d, the peak intensity of the CNS-Fe catalyst appears more similar to that of the Fe foil, suggesting that metallic Fe is also present in the core. Therefore, the iron species in the core of CNS likely contains Fe_3O_4, Fe_2O_3 and metallic Fe, which was confirmed by H_2-TPR and further characterization of XRD.

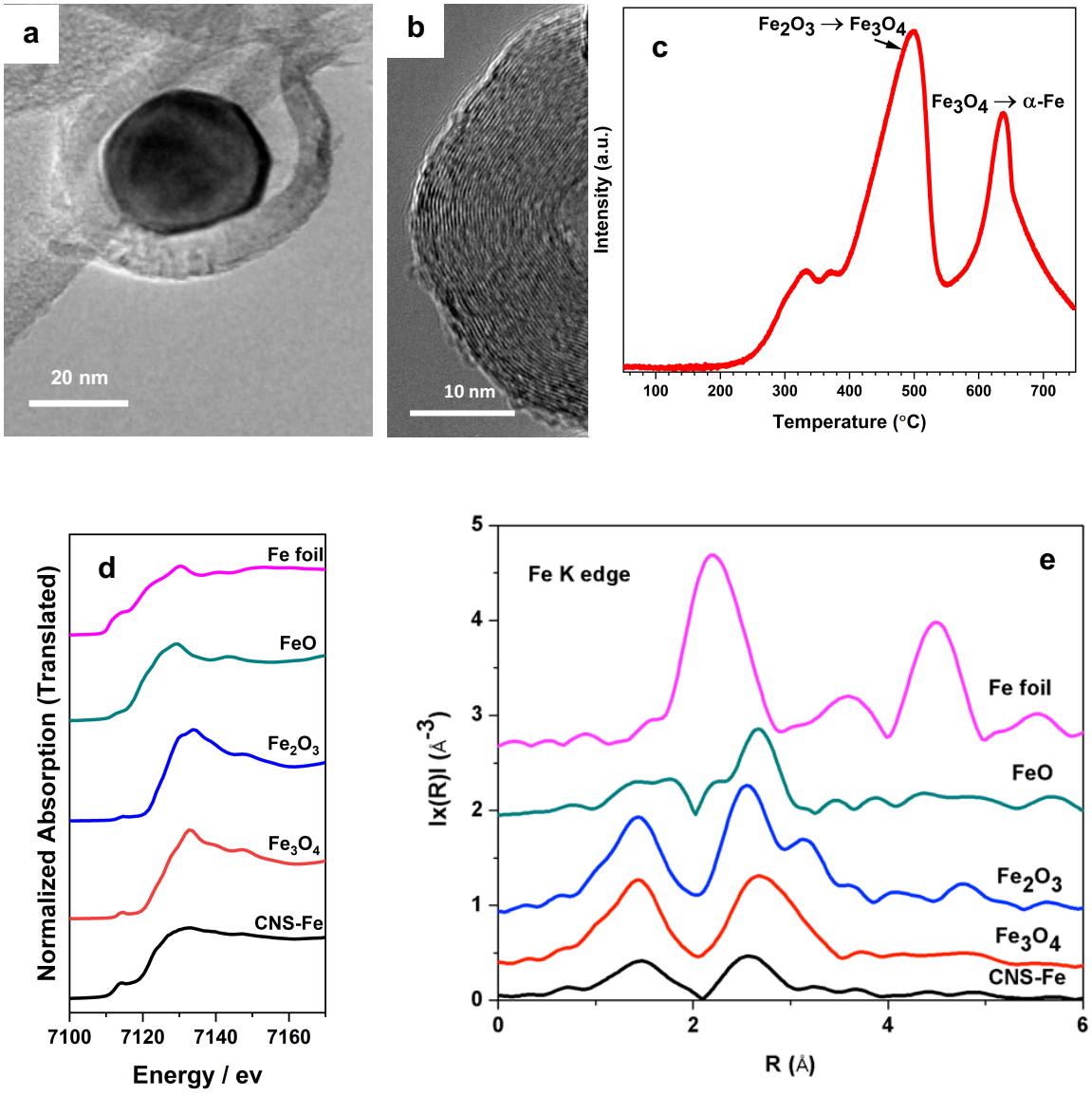

Figure 1. Physicochemical properties of fresh CNS-Fe, a) TEM of CNS-Fe core-shell structure, b) TEM of graphitic laye in the shell of CNS-Fe, c) H_2-TPR of CNS-Fe, (d) Normalized XANES of CNS-Fe with reference compounds at the Fe K-edge, e) Fourier transform of the experimental EXAFS spectra of CNS-Fe (phase-uncorrected).

3.3 Catalyst Evaluation for CO_2 Hydrogenation

The synthesized CNS-Fe (7.2 wt%) was evaluated using a flow bed reactor at ambient pressure. Iron time yield (FTY) in $\mu mol_{CO2} \cdot g_{Fe}^{-1} \cdot s^{-1}$ as a function of temperature and time on stream are graphically presented in Figure 2a. At each temperature, six GC injections were conducted and therefore six data points were collected for product analysis. As shown in Figure 2a, the FTY increased as temperature increased from 250 to 400 °C and reached 1900 $\mu mol_{CO2} \cdot g_{Fe}^{-1} \cdot s^{-1}$ at maximum. The gradual decrease in FTY at 350 °C indicated catalyst deactivation at higher temperatures. The hydrocarbon (C_2-$C_4^=$, C_2-C_4^0, CH_4, C_{5+}) distribution, CO_2 conversion and CO selectivity as a function of temperature are depicted in Figure 2b for CNS-Fe (7.2 wt%). As the temperature increased from 275 to 400 °C, CO_2 conversion increased, together with the C_2-$C_4^=$ distribution in the hydrocarbons, but the C_2-C_4^0 distribution decreased, indicating that higher temperature favored the light olefin production while lower temperature favored the C_2-C_4^0 production among the hydrocarbons. Furthermore, higher temperatures promoted the CO production as the main product. At 350 °C, the conversion of CO_2 to products could also be accompanied by the carbonization of Fe_2O_3 and Fe_3O_4, as evidenced by XRD of the spent catalyst, which is further discussed below. Once Fe_5C_2 was formed, the catalyst performance appeared more stable. The less drop in FTY at 400 °C could be due to the formation of carbide at 350 °C.

CNS-Fe catalysts with Fe content of 16.3 and 16.4 wt% were also tested for CO_2 hydrogenation under the same testing conditions as shown in Figure 2a and Figure S1a. As mentioned earlier, the Fe content in the CNS could reach a saturation point even though larger amount of iron complex precursor was applied during the synthesis of the CNS-Fe (16.3 vs. 16.4 Fe wt%). The catalysts with higher Fe content showed more stable performance at higher reaction temperature. The lower FTY values for the CNS-Fe catalysts with 16.3 and 16.4 wt% Fe content with respect to that of the catalyst with 7.2 wt% Fe is due to lower surface-to-weight ratio of the Fe species inside the CNS inner space. While the CO_2 conversion was higher for the higher Fe content (16.3 and 16.4 wt%) catalysts than for the catalyst with 7.2 wt% Fe, the FTY values were calculated by normalizing the converted CO_2 over the Fe contents, resulting in lower FTY values for the CNS-Fe catalysts with 16.3 and 16.4 wt% Fe (Figure 2a and Figure S1a). While the 16.3 and 16.4 wt% Fe CNS-Fe catalysts showed similar conversions and product selectivities, difference in hydrocarbon distributions between the catalysts having high Fe content and that having 7.2 wt% Fe was observed (Figure 2b-c and Figure S1b): (1) The C_2^+ products are higher with the CNS-Fe catalysts having higher Fe content than the one having 7.2 wt% Fe, and (2) the olefins are higher for the catalysts at higher Fe content.

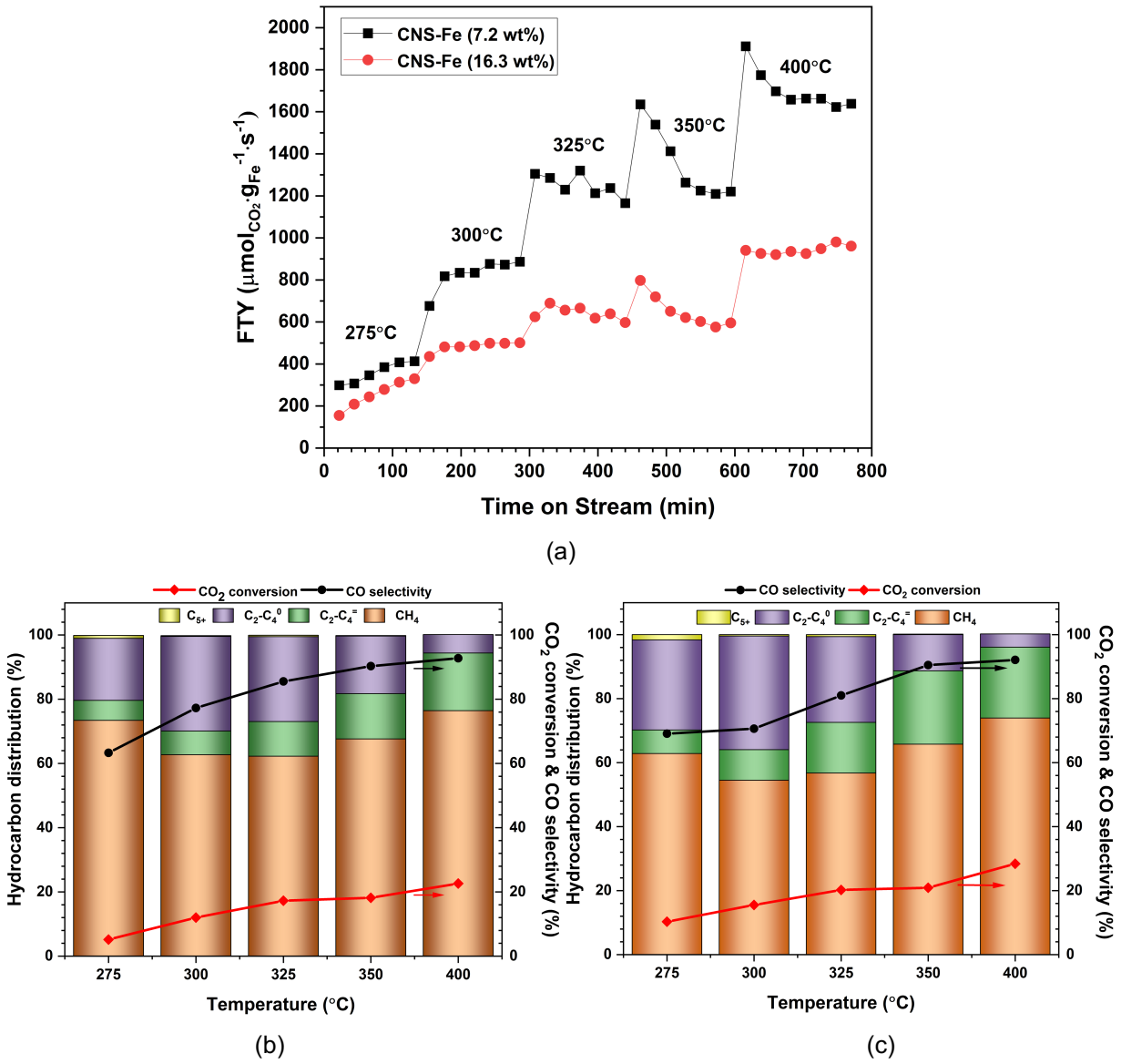

Figure 2. Catalytic performance of CNS-Fe. (a) CO_2 hydrogenation catalytic performance (FTY in $\mu mol_{CO2} \cdot g_{Fe}^{-1} \cdot s^{-1}$) on time on stream (TOS) over CNS-Fe core-shell catalyst with varying Fe content. (b-c) CO_2 hydrogenation catalytic performance (hydrocarbon distribution, CO_2 conversion and CO selectivity) as a function of temperature for (b) CNS-Fe (7.2 wt%) core-shell catalyst and (c) CNS-Fe (16.3 wt%) core-shell catalyst. Testing Conditions: Temperature: 275~400 °C; GHSV: 24000 mL $g^{-1} \cdot h^{-1}$; H_2/CO_2 = 3:1, P: atmospheric pressure.

Figure 3a shows the effect of varying H_2/CO_2 volume ratios on the CO_2 conversion (275~400 °C). The CO_2 conversion increased with temperature from 275 to 400 °C at decreasing H_2/CO_2 ratio. Figure 3b shows the effect of varying H_2/CO_2 volume ratios on hydrocarbon distribution at 400 °C. With decreasing H_2/CO_2 ratio, the CO_2 conversion at 400 °C decreased as expected. The selectivity of CO as a main product was rapidly increased with the decreasing H_2/CO_2 volume ratios, due to less available H_2. The selectivity of hydrocarbon products became insignificant due to poor CO conversion. While CO accounted for ~98% of the products in CO_2 hydrogenation with H_2/CO_2 ratio of 1:1, CO accounted for ~90% of the products with

H_2/CO_2 ratio of 3:1. Although higher H_2/CO_2 ratio favors more hydrocarbon products, a ratio of 3:1 did not show markedly difference from that of 5:1 in hydrocarbon distribution. Furthermore, the stoichiometric ratio between H_2 and CO_2 to produce olefins was 3:1. Therefore, the test for the catalytic CO_2 hydrogenation was conducted mostly at H_2/CO_2 ratio of 3:1 as shown in the testing conditions in Figure 2. To gain insight into the relationship between catalytic activity and the CNS-Fe structure, XRD, XPS, Raman and TGA studies were used to investigate the fresh and spent CNS-Fe (7.2 wt%) catalysts. It should be noted that almost no C_{5+} hydrocarbons were produced using CNS-Fe under various testing conditions in this work. On the contrary, C_{5+} species were produced using CNT-Fe, possibly from diffusion-limited side reactions due to higher aspect ratios of the CNT support.[63,64] It has been confirmed both experimentally and theoretically in literature that the high aspect induced diffusion channels in CNTs led to side reactions producing C_{5+} species.[63] Mattia et al. produced 3.5% C_{5+} hydrocarbons using Fe@CNT at 370 °C and a H_2/CO_2 ratio of 3:1, confirming the effect of diffusion-limited side reactions.[64] The relatively lower CO_2 conversion with CNS-Fe compared to those with CNT-Fe is likely caused by the larger Fe core (~40 nm) in CNS (Fe particles in CNT are below 10 nm) instead of the higher aspect ratios of the CNT support.

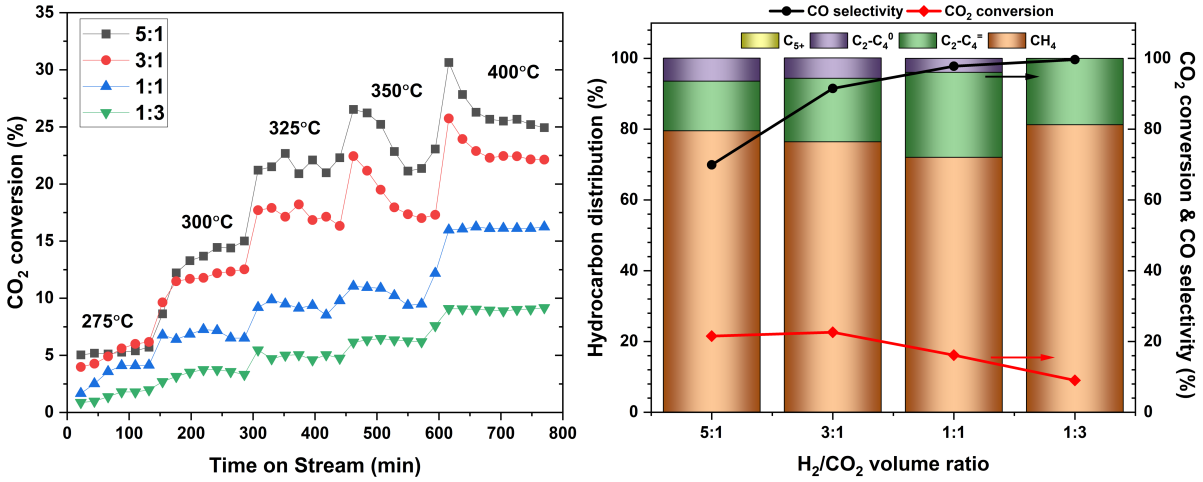

(a) (b)

Figure 3. (a) CO_2 conversion on time on stream over CNS-Fe (7.2 wt%) core-shell catalyst with varying CO_2/H_2 volume ratio. Testing Conditions: Temperature: 275~400 °C; GHSV: 24000 mL g-1·h-1; catalyst: CNS-Fe (7.2 wt%); P: atmospheric pressure. (b) CO_2 hydrogenation catalytic performance (hydrocarbon distribution, CO_2 conversion and CO selectivity) as a function of H_2/CO_2 volume ratio at 400 °C. Testing Conditions: GHSV: 24000 mL $g^{-1}\cdot h^{-1}$; catalyst: CNS-Fe (7.2 wt%); P: atmospheric pressure.

3.4 Physicochemical Properties of Fresh and Spent CNS-Fe

Figure 4 shows the diffractograms of the fresh CNS-Fe before activation and the spent catalyst after hydrogenation in the range of 10 to 70°. The XRD patterns can be indexed to a mixture of carbon, Fe_2O_3, Fe_3O_4, Fe_5C_2, and Fe as denoted in XRD. The broad peaks in the range of 10-20° characteristic of amorphous carbon indicated the small amount of amorphous carbon (defects) on CNS. The sharp peak at 2θ = 26° is ascribed to the (002) plane of graphite (PDF 00-41-1487).[65] The doublet at 2θ =24°, as shown

in the magnified image, belongs to the Fe_2O_3 (210, 211) planes. The diffraction peaks at 2θ = 15.0, 18.4, 26.1, 30.3, 35.7, 40.9, 49.5, and 53.9° correspond to the (110), (111), (211), (220), (311), (321), (421), and (422) crystal facets of Fe_2O_3, respectively (PDF 00-039-1346). The diffraction peaks at 2θ = 30.1, 35.4, 57.2, and 62.9° are attributed to the (220), (311), (511), and (440) crystal facets of Fe_3O_4, respectively (PDF 00-065-0731). The peak at 2θ = 42.6 corresponds to the (110) plane of metallic Fe (PDF 00-006-0696). The peak at 2θ = 43.4 is assigned to the (112) plane of Fe_5C_2 (PDF 00-051-0997). In the spent CNS-Fe, the intensity of the peaks for graphite and Fe_3O_4 significantly decreased, and the peaks for Fe_2O_3 almost disappeared. It is interesting to note that the peak for iron carbide Fe_5C_2 drastically increased, which indicated that χ-Fe_5C_2 was the active site for the CO_2 hydrogenation, further proving the high FTY for the catalytic performance.

In the carbonization step for the synthesis of fresh CNS-Fe, the graphite layer was formed as the shell of the CNS, and the diffusion of graphitic carbon to the core Fe_xO_y is slow. During the reaction, the carbonaceous intermediates in CO_2 hydrogenation leading to the formation of CO and olefins would also likely further carbonize Fe, forming the Fe_5C_2 phase, as evidenced by the nearly complete disappearance of Fe_2O_3 and the large decrease of Fe_3O_4 in Figure 4.

The XRD data confirmed that the iron species (Fe_3O_4, metallic Fe and iron carbide χ-Fe_5C_2) encapsulated within the nano-cavity of CNS were protected and retained a more reduced state than fully oxidized Fe_2O_3. The disappearance of Fe_2O_3 and the dominant formation of χ-Fe_5C_2 in the spent catalyst resembled a favorable balance of these iron species in catalyzing the sequence of reactions in Eqns. 1-4 above. The *in-situ* carbonization of Fe_xO_y by the mobile carbonaceous intermediates during the initial reaction appeared to play a beneficial role in forming a more active and stable balance of the iron species. As revealed by TEM and XRD, CNS-Fe was a core-shell architecture. It is composed of a mixture of Fe, Fe_3O_4, χ-Fe_5C_2 in the core and graphitic carbon rich in defects in the shell.

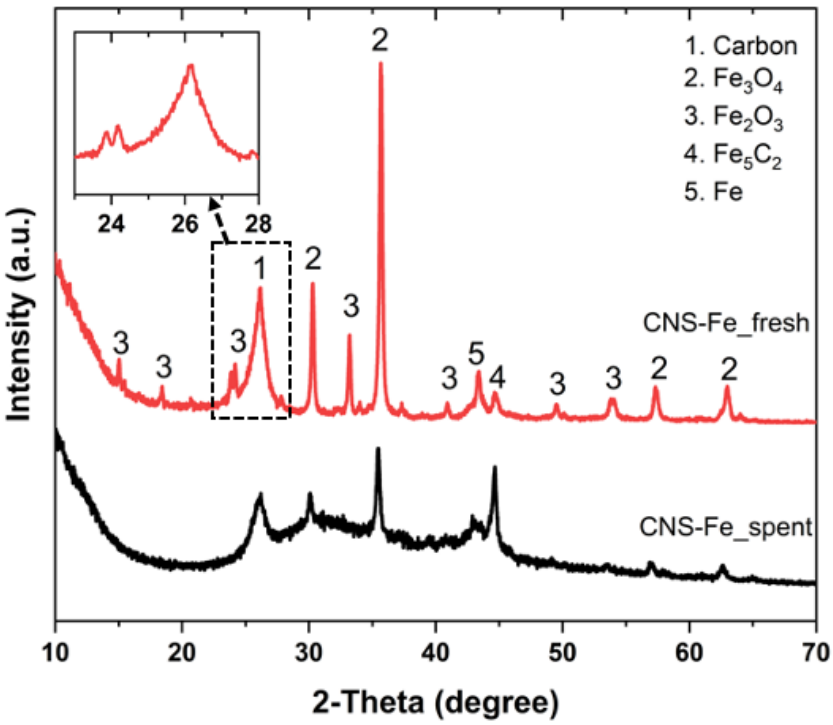

Figure 4. XRD of fresh and spent CNS-Fe core-shell catalysts.

XPS was used to characterize the structures of the surface layers. XPS spectra for the Fe 2p of fresh and spent CNS-Fe are presented in Figure 5a-b. For XPS, the fitting parameters are based on XRD detection of different Fe species. The 710.0 eV and 712.2 eV peaks are attributed to Fe (II) and Fe (III), respectively. The shake-up satellite peaks of Fe (II) ($2p_{3/2}$) and Fe (III) ($2p_{3/2}$) are observed at 715.4.8 eV and 718.9 eV, respectively. The peaks at 720-730 eV in both the fresh and spent CNS-Fe catalysts correspond to the binding energy of Fe $2p_{1/2}$. The Fe 2p energy level gives rise to a doublet with different binding energies, Fe $2p_{1/2}$ and Fe $2p_{3/2}$, due to spin-orbital splitting. The binding energies for Fe (II) and Fe (III) are similar to that of Fe_3O_4.[66] The Fe 2p peak at 708.2 eV indicates the presence of χ-Fe_5C_2 in the fresh CNS-Fe.[67] This χ-Fe_5C_2 species, also evidenced in the XRD pattern of Figure 6, was expected as the initial active catalyst for CO-FTS (Eqn. 2). In the spent CNS-Fe, the increased peak intensity at 708.2 eV suggests increased surface iron carbide (χ-Fe_5C_2) after CO_2 hydrogenation, which was also consistent with the XRD pattern (Figure 5). Peak at 709.1 eV for metallic Fe in fresh sample was decreased in intensity in spend sample, likely due to the carbonization of the increased χ-Fe_5C_2 species (Figure 5b) during the reaction.[68] The C1s spectra of fresh and spent CNS-Fe shown in Figure 5c-d consist of six peaks attributed to χ-Fe_5C_2 (283.2 eV), sp^2 graphitic carbon (284.6 eV), C-C bond (285.7 eV), -C-O- bond (286.7 eV), C=O bond (289.1 eV), and shake-up feature (291.3 eV), respectively.[48] In the fresh sample, the higher intensity in graphite peak confirmed the high graphitization degree of the carbon shell in the CNS-Fe as confirmed by the TEM and XRD. The decrease of the intensity in the graphite peak for the spent sample indicated more amorphous carbon deposition, resulting in the catalyst deactivation. The O1s spectra of fresh and spent CNS-Fe shown

in Figure S2a-b are composed of three peaks corresponding to Fe-O (530.1 eV), C-O (532.0 eV), and C=O (533.7 eV), respectively. In the spent catalyst, one extra peak appeared and is attributed to adsorbed water formed during the CO_2 hydrogenation.

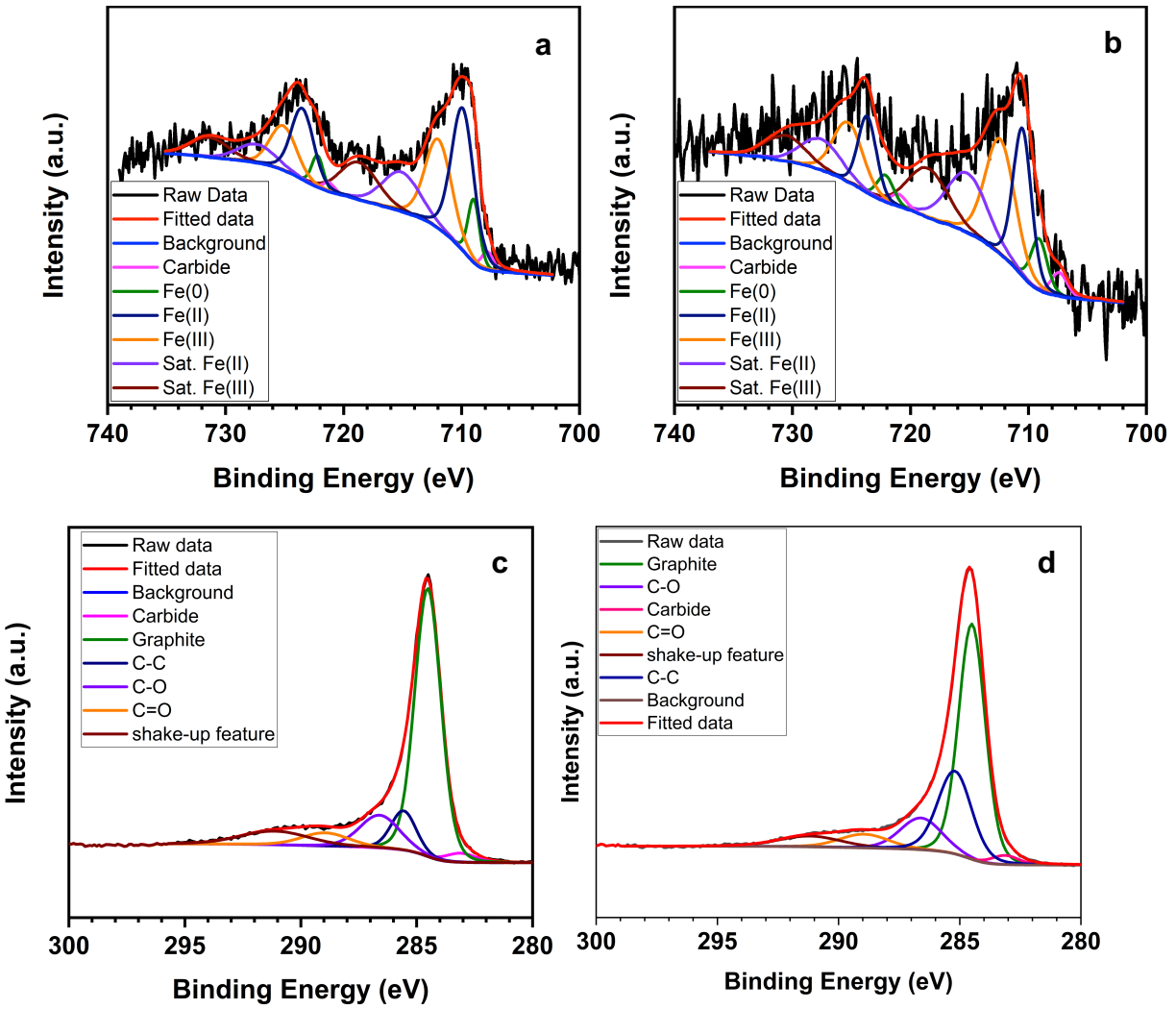

Figure 5. XPS spectra of CNS-Fe. (a,b) Fe 2p spectra of (a) fresh and (b) spent samples; (c,d) C1s spectra of (c) fresh and (d) spent samples

The fresh and spent CNS-Fe samples were analyzed by Raman spectroscopy and exhibited in Figure 6a. The peaks appeared at 215, 276, 398, and 654 cm^{-1} were ascribed to Fe_3O_4, which had identical features to Fe_3O_4 nanoparticles reported.[69-71] This further confirmed that the Fe_3O_4 encapsulated in CNS were in the scale of nanometer. The peak at 1585 cm^{-1} (G-band) appeared in sharp shape was attributed to the in-plane vibrations of graphene sheet E_{2g} zone-center mode.[72] The peak at 2700 cm^{-1} (G'-band) referred to the stacking order of graphene layers.[73] The peak at 1358 cm^{-1} (D-band) corresponded to the defects and edge planes. The presence of relatively strong D band indicated the rich presence of defects. The defects in the form of mesoporous CNS could be essential in opening up the accessibility of reactant molecules to the active sites in the core. As shown in the Raman spectra, there is no significant difference

between the fresh and spent CNS-Fe catalysts, indicating that no significant changes occurred for the core-shell structure before and after the CO_2 hydrogenation.

Thermo-gravimetric analysis (TGA) for the fresh and spent CNS-Fe catalysts was compared in Figure 6b. It shows that the total weight loss of fresh CNS-Fe was less than 3 % while it was more than 4.5 % for the spent sample. The more weight loss for the spent CNS-Fe was probably due to the carbon deposition after the CO_2 hydrogenation. The weight loss for fresh CNS-Fe started at ca. 450 °C while the weight loss for spent CNS-Fe started at ca. 550 °C. This could indicate some formation of iron carbide which had a high thermal stability. Furthermore, the carbon deposited on the spent sample was graphitic. The shell structure is mainly composed of graphitic carbon with some defect sites as confiremed by XRD and TEM. The XRD, TGA and Raman studies of the fresh and spent catalysts confirmed the stability of the carbon shell.

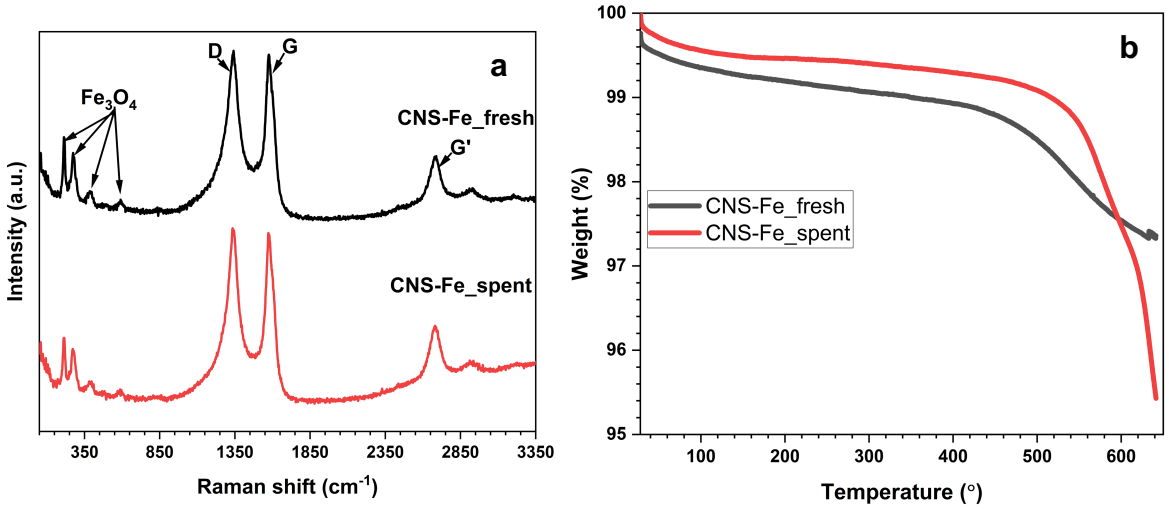

Figure 6. (a) Raman and (b) TGA of fresh and spent CNS-Fe

3.4 Rationale of Reaction Mechanism

In view of the formation mechanism of light olefins, a key point was to control the H/C to a suitable ratio, in which too much surface H* could cause further hydrogenation to saturated hydrocarbons and methane, whilst the contrary condition would cancel out the hydrogenation ability and lessen the activity in CO_2 and intermediate CO conversions. The vital step of light olefins synthesis by CO_2 hydrogenation is C–O bond cleavage and C–C bond formation.[42,43] In this work, our results indicate that a H_2/CO_2 ratio of 3:1 is optimal without the need for excessive H_2.

Through CO_2-FTS process over Fe-based catalysts, the primary Fe_2O_3 phase is reduced by hydrogen to Fe_3O_4, which is the active phase for the RWGS reaction and can be further reduced to Fe in metallic state [52,53,73] as confirmed by XRD, XPS and H_2-TPR. The reaction mechanism for the CO_2-FTS

pathway is suggested previously.[43] Carboxylate species (*CO_2, * representing the adsorbed state) was formed after CO_2 is absorbed and activated on the active phases (e.g., Fe_3O_4) for RWGS. The adsorbed H can hydrogenate the resulted *CO_2 to form an *HOCO intermediate, which further dissociates into *CO and *OH species. The *CO dissociates into *O and *C. Some of the produced *C can diffuse into the metal lattice to form metal carbides such as χ-Fe_5C_2, the active phase for the FTS reaction,[70] as confirmed by XRD and XPS in this work. The C* on the χ-Fe_5C_2 surface may be then hydrogenated to CH_x* species. C*+CH_x* and CH_x*+CH_x* were the most likely coupling pathways.[74]

The core-shell nano-environment formed by encapsulating the active Fe species in CNS provided a good model system to explore the fundamentals of confined catalysis. As illustrated in the Scheme 2, the reactant gases CO_2 and H_2 diffused through the defects of the carbon shell into the core and contacted with Fe_3O_4 to form intermediate CO, which further accessed to the active sites (metallic Fe and iron carbide Fe_5C_2) to form light olefins. As mentioned above, Fe_3O_4 was reported to favor reverse water gas shift reaction, and Fe_5C_2 was the active site for converting CO to light olefins. In this work, the major by-product CO was formed probably due to the larger amount of Fe_3O_4 and limited amount of Fe_5C_2 in the core of the CNS for the efficient conversion of CO_2 to light olefins. Future work will focus on investigating the factors that affect the conversion of Fe_3O_4 to iron carbide Fe_5C_2 in the core of CNS. The effect of promoters will also be investigated to improve CO intermediate conversion and to reduce CH_4 formation.

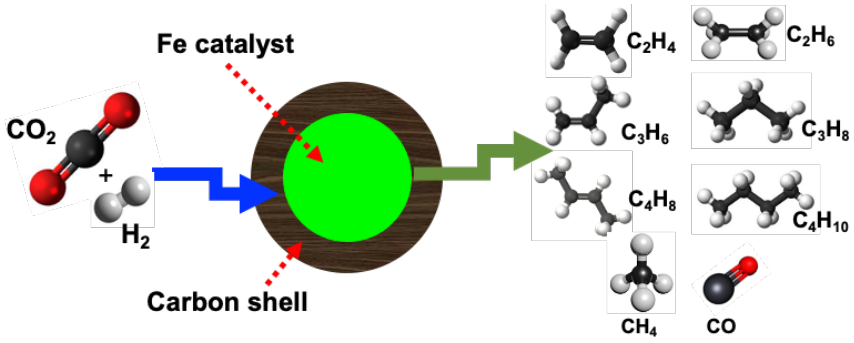

Scheme 2. Illustration of CO_2 hydrogenation over CNS-Fe.

Fe precursor plays an important role in the synthesis of the CNS core-shell structure. In addition, as demonstrated in this work, the structure of Fe species and the reaction conditions are important to the product selectivity. Tuning the structures of iron based catalysts, i.e. Fe_3O_4, metallic Fe and Fe_5C_2, in the core of the CNS is critically important to the selectivity of CO_2 hydrogenation. This work shows a method to prepare CNS encapsulated Fe oxides species and the transformation of the oxides to active Fe species that demonstrates catalytic activity for CO_2 hydrogenation under ambient pressure. Further tuning the Fe species and evaluating the catalysts at higher pressures are the objectives of future research.

4. Conclusions

CNS-Fe was synthesized using an iron precursor (IPC) as a template and dispersant during the resorcinol-formaldehyde polymerization process, followed by carbonization. The synthesized CNS-Fe was

characterized using SEM, TEM, H_2-TPR, XANES, EXAFS, XRD, XPS, Raman and TGA to determine the morphologies and structures. The synthesized CNS-Fe was determined to have spherical carbon nanostructures with the core at ca. 40 nm and shell thickness of ca. 10 nm. The fresh CNS-Fe contained a mixture of Fe_3O_4, metallic Fe and iron carbide Fe_5C_2 in the core and a shell as graphitic and rich in defect sites. The catalytic performance evaluated based on FTY, hydrocarbon distribution, CO_2 conversion and CO selectivity as a function of time on stream, temperature, and CO_2/H_2 flow ratio suggests CNS-Fe as a promising catalyst for CO_2 hydrogenation to light olefins. The core-shell nano-environment formed by encapsulating the active Fe species in CNS provides a unique model system to study the fundamentals of confined catalysis. Future theoretical calculations of the reaction pathways should provide more insight into the active sites responsible for the experimental results reported in this study.

ASSOCIATED CONTENT

Supporting Information Available: CO_2 hydrogenation catalytic performance (FTY in $\mu mol_{CO2} \cdot g_{Fe}^{-1} \cdot s^{-1}$) on time on stream (TOS) over CNS-Fe core-shell catalyst with varying Fe content; CO_2 hydrogenation catalytic performance (hydrocarbon distribution, CO_2 conversion and CO selectivity) as a function of temperature for CNS-Fe (16.4 wt%) core-shell catalys; XPS spectra of fresh and CNS-Fe at O1s region.

Author Contributions: Conceptualization, C.Z.; writing-original draft, C.Z.; catalyst synthesis and testing, D.W. and A.S.; XPS and H_2-TPR, N.R.; EXAFS, F.Z.; XRD, D.V.; Raman, H.Z.; iron content determination and TGA, P.L., M.W. and K.A.; writing-review and editing, C.Z. P.L., J.Z.Z and S.D.S.; funding acquisition, C.Z.; re-sources, C.Z.; supervision, C.Z. All authors have read and agreed to the published version of the manuscript.

Funding: This work was supported by the National Science Foundation (NSF) under Grant No. 1955521 (CZ) and NSF-MRI Grant No. DMR-2116353 (PL). PL was supported by Rowan University New Faculty Startup Fund (PL), Rowan CATALYST Funding Program. The research carried out at Brookhaven National Laboratory was supported by the U.S. Department of Energy, Office of Science and Office of Basic Energy Sciences under contract No. DE-SC0012704. SDS was supported by a U.S. DOE Early Career Award.

Acknowledgments

The authors are grateful for the U.S. Department of Energy, Office of Science, Office of Workforce Development for Teachers and Scientists under the Visiting Faculty Program (CZ).

Conflicts of Interest: The authors declare no conflict of interest.

References

1. Zhang, X.; Zhang, A.; Jiang, X.; Zhu, J.; Liu, J.; Li, J.; Zhang, G.H.; Song, C.S; Guo, X.W. Utilization of CO_2 for aromatics production over ZnO/ZrO_2-ZSM-5 tandem catalyst. *J. CO_2 Util.* **2019**, *29*, 140-145. DOI: 10.1016/j.jcou.2018.12.002

2. Centi, G.; Quadrelli, E.A.; Perathoner, S. Catalysis for CO_2 conversion: A key technology for rapid introduction of renewable energy in the value chain of chemical industries. *Energy Environ. Sci.* **2013**, *6*, 1711–1731. DOI: 10.1039/C3EE00056G
3. Dowell, N.M.; Fennell, P.S.; Shah, N.; Maitland, G.C. The role of CO_2 capture and utilization in mitigating climate change. *Nat. Clim. Change* **2017**, *7*, 243–249. DOI: 10.1038/nclimate3231
4. Chen, H.; Liu, J.; Liu, P.; Wang, Y.; Xiao, H.; Yang, Q.; Feng, X.; Zhou, S. Carbon-confined magnesium hydride nano-lamellae for catalytic hydrogenation of carbon dioxide to lower olefins. *J. Catal.* **2019**, *379*, 121−128. DOI: 10.1021/acscatal.0c01579
5. Ma, Z.; Porosoff, M. Development of tandem catalysts for CO_2 hydrogenation to olefins. *ACS Catal.* **2019**, *9*, 2639−2656. DOI: 10.1021/acscatal.8b05060
6. Science Daily. Available Online: https://www.sciencedaily.com/releases/2018/11/181108130533.htm.
7. Galvis, H.M.T.; de Jong, K.P. Catalysts for production of lower olefins from synthesis gas: A review. *ACS Catal.* **2013**, *3*, 2130−2149. DOI: 10.1021/cs4003436
8. Wei, J.; Ge, Q.J.; Y.R.W.; Wen, Z.Y.; Fang, C.Y.; G. L. S.; Xu, H.Y.; Sun, J. Directly converting CO_2 into a gasoline fuel. *Nat. Commun*. **2018**, *8*, 15174. DOI: 10.1038/ncomms15174
9. Li, Z.L.; Qu, Y.Z.; Wang, J.J.; Liu, H.L.; Li, M.R.; Miao, S.; Li, C. Highly selective conversion of carbon dioxide to aromatics over tandem catalysts. *Joule* **2019**, *3*, 570−583. DOI: 10.1021/acscentsci.0c00976
10. Xie, C.L.; Chen, C.; Yu, Y.; Su, J.; Li, Y.F.; Somorjai, G.A.; Yang, P.D. Tandem catalysis for CO_2 hydrogenation to C_2−C_4 hydrocarbons. *Nano Lett.* **2017**, *17*, 3798−3802. DOI: 10.1021/acs.nanolett.7b01139
11. Liu, M.; Yi, Y.H.; Wang, L.; Guo, H.C.; Bogaerts, A. Hydrogenation of carbon dioxide to value-added chemicals by heterogeneous catalysis and plasma catalysis. *Catalysts* **2019**, *9*, 275. DOI: 10.3390/catal9030275
12. Dang, S.S.; Gao, P.; Liu, Z.Y.; Chen, X.Q.; Yang, C.G.; Wang, H.; Zhong, L.S.; Li, S.G.; Sun, Y.H. Role of zirconium in direct CO_2 hydrogenation to lower olefins on oxide/zeolite bifunctional catalysts. *J. Catal*. **2018**, *364*, 382−393. DOI: 10.1016/j.jcat.2018.06.010
13. Gnanamani, M.K.; Jacobs, G.; Hamdeh, H.H.; Shafer, W.D.; Liu, F.; Hopps, S.D.; Thomas, G.A.; Davis, B.H. Hydrogenation of carbon dioxide over Co−Fe bimetallic catalysts. *ACS Catal.* **2016**, *6*, 913−927. DOI: 10.1021/acscatal.5b01346
14. Wang, D.; Xie, Z.; Porosoff, M.D.; Chen, J. Recent advances in carbon dioxide hydrogenation to produce olefins and aromatics. *Chem* **2021**, 7, 1−35. DOI: 10.1016/j.chempr.2021.02.024
15. Liu, J. H.; Zhang, A. F.; Jiang, X.; Liu, M.; Zhu, J.; Song, C. S. and Guo, X. W. Direct transformation of carbon dioxide to value-added hydrocarbons by physical mixtures of Fe_5C_2 and K-modified Al_2O_3, *Ind. Eng. Chem. Res*. **2018**, *57*, 9120-9126. DOI: 10.1021/acs.iecr.8b02017
16. Xie, C. L.; Chen, C.; Yu, Y.; Su, J.; Li, Y. F.; Gabor A. Somorjai, G. A.; Yang, P. D. Tandem Catalysis for CO_2 Hydrogenation to C2−C4 Hydrocarbons. *Nano Lett.* **2017**, *17*, 3798-3802. DOI: 10.1021/acs.nanolett.7b01139
17. Gao, P.; Dang, S. S.; Li, S. G.; Bu, X. N.; Liu, Z. Y.; Qiu, M. H.; Yang, C. G.; Wang, H.; Zhong, L. S.; Han, Y.; Qiang Liu, Q.; Wei, W.; Sun, Y. H. Direct production of lower olefins from CO_2 conversion via bifunctional catalysis. *ACS Catal.* **2018**, *8*, 571-578. DOI: 10.1021/acscatal.7b02649
18. You, Z. Y.; Deng, W. P.; Zhang, Q. H.; Wang, Y. Hydrogenation of carbon dioxide to light olefins over non-supported iron catalyst, *Chinese J. Catal.* **2013**, *34*, 956-963. DOI: 10.1016/S1872-2067(12)60559-2
19. Porosoff, M. D.; Chen, J. G. Trends in the catalytic reduction of CO_2 by hydrogen over supported monometallic and bimetallic catalysts. *J. Catal.* **2013**, *301*, 30-37. DOI: 10.1016/j.jcat.2013.01.022

20. Prieto, G. Carbon dioxide hydrogenation into higher hydrocarbons and oxygenates: Thermodynamic and kinetic bounds and progress with heterogeneous and homogeneous catalysis. *Chem. Sus. Chem*. **2017**, *10*, 1056-1070. DOI: 10.1002/cssc.201601591
21. Visconti, C. G.; Martinelli, M.; Falbo, L.; Infantes-Molina, A.; Lietti, L.; Forzatti, P.; Iaquaniello, G.; Palo, E.; Picutti, B.; Brignoli, F. CO_2 hydrogenation to lower olefins on a high surface area K promoted bulk Fe-catalyst. *Appl. Catal. B*. **2017**, *200*, 530-542. DOI: 10.1016/j.apcatb.2016.07.047
22. Li, W.; Zhang, A.; Jiang, X.; Janik, M. J.; Qiu, J.; Liu, Z.; Guo, X.; Song, C. The anti-sintering catalysts: Fe−Co−Zr polymetallic fibers for CO_2 hydrogenation to C2=-C4=-rich hydrocarbons. *J. CO_2 Util.* **2018**, *23*, 219-225. DOI: 10.1016/j.jcou.2017.07.005
23. Gnanamani, M. K.; Hamdeh, H. H.; Shafer, W. D.; Hopps, S. D.; Davis, B. H. Hydrogenation of carbon dioxide over iron carbide prepared from alkali metal promoted iron oxalate. *Appl. Catal. A* **2018**, *564*, 243-249. DOI: 10.1016/j.apcata.2018.07.034
24. Kattel, S.; Yu, W.; Yang, X.; Yan, B.; Huang, Y.; Wan, W.; Liu, P.; Chen, J. G. CO_2 hydrogenation over oxide-supported PtCo catalysts: The role of the oxide support in determining the product selectivity. *Angew. Chem. Int. Ed.* **2016**, *55*, 7968-7973. DOI: 10.1002/anie.201601661
25. Cui, T.; Dong, J. H.; Pan, X. L.; Yu, T.; Fu, Q.; Bao, X. H. Enhanced hydrogen evolution reaction over molybdenum carbide nanoparticles confined inside single-walled carbon nanotubes. *J. Energy Chem*. **2019**, *28* 123-127. DOI: 10.1016/j.jechem.2018.03.006
26. Xiao, J. P.; Pan, X. L.; Guo, S. J.; Ren, P. J.; Bao, X. H. Toward Fundamentals of Confined Catalysis in Carbon Nanotubes. *J. Am. Chem. Soc*. **2015**, *137*, 477-482. DOI: 10.1021/ja511498s
27. Li, S. W.; Tuel A.; Meunier, F.; Aouine, M.; Farrusseng, D. Platinum nanoparticles entrapped in zeolite nanoshells as active and sintering-resistant arene hydrogenation catalysts. *J. Catal.* **2015**, *332*, 25-30. DOI: 10.1016/j.jcat.2015.09.006
28. Wang, T. S.; Gao, L. J.; Hou, J. W.; Herou, S. J. A.; Griffiths, J. T.; Li, W. W.; Dong, J. H.; Song Gao, S.; Titirici, m. M.; Kumar, R. V.; Cheetham, A. K.; Bao, X. H.; Fu, Q.; Smoukov S. K. Rational approach to guest confinement inside MOF cavities for low-temperature catalysis. *Nat. Commun.* **2019**, *10*, 1340. DOI: 10.1038/s41467-019-08972-x
29. Jiang, K.; Siahrostami, S.; Zheng, T. T.; Hu, Y. F.; Hwang, S.; Stavitski, E.; Peng, Y.; Dynes, J.; Gangisetty, M.; Su, D., Attenkofer, K.; Wang, H. T. Isolated Ni single atoms in graphene nanosheets for high-performance CO_2 reduction. *Energy Environ. Sci.* **2018**, *4*. DOI: 10.1039/C7EE03245E
30. Zhan, G.; Zeng, H. C. ZIF-67-derived nanoreactors for controlling product selectivity in CO_2 hydrogenation. *ACS Catal*. **2017**, *7*, 7509-7519. DOI: 10.1021/acscatal.7b01827
31. Wang, X. F.; Cui, Y. Z.; Wang, Y.; Song, X. W.; Yu, J.H. Fabrication and Catalytic Performance of Highly Stable Multifunctional Core−Shell Zeolite Composites. *Inorg. Chem*. **2013**, *52*, 10708-10710. DOI: 10.1021/ic401357s
32. He, J. J.; Liu, Z. L.; Yoneyama, Y.; Nishiyama, N.; Tsubaki, N. Multiple-Functional Capsule Catalysts: A Tailor-Made Confined Reaction Environment for the Direct Synthesis of Middle Isoparaffins from Syngas. *Chem. Eur. J*. **2006**, *12*, 8296-8304. DOI: 10.1002/chem.200501295
33. Ren, N.; Yang, Y. H.; Shen, J.; Zhang, Y. H.; Xu, H. L.; Gao, Z.; Tang, Y. Novel, efficient hollow zeolitically microcapsulized noble metal catalysts. *J. Catal*. **2007**, *251*, 182-188. DOI: 10.1016/j.jcat.2007.07.009
34. Yang, G. H.; Kawata, H.; Lin, Q. H.; Wang, J. Y.; Jin, Y. Z.; Zeng, C. Y.; Yoneyama Y.; Tsubaki, N. Oriented synthesis of target products in liquid-phase tandem reaction over a tripartite zeolite capsule catalyst. *Chem. Sci.,* **2013**, *4*, 3958. DOI: 10.1039/C3SC51499D

35. Goel, S.; Wu, Z. J.; Stacey I.; Zones, S. I.; Iglesia, E. Synthesis and Catalytic Properties of Metal Clusters Encapsulated within Small-Pore (SOD, GIS, ANA) Zeolites. *J. Am. Chem. Soc.* **2012**, *134*, 17688-17695. DOI: 10.1021/ja307370z
36. Gu, J.; Zhang, Z. Y.; Hu, P.; L. P.; Xue, N. H.; Peng, L. M.; Guo, X. F.; Lin, M.; Ding, W. P. Platinum Nanoparticles Encapsulated in MFI Zeolite Crystals by a Two-Step Dry Gel Conversion Method as a Highly Selective Hydrogenation Catalyst. *ACS Catal.* **2015**, *5*, 6893-6901. DOI: 10.1021/acscatal.5b01823
37. Farrusseng, D.; Tuel, A. Perspectives on zeolite-encapsulated metal nanoparticles and their applications in catalysis. *New J. Chem*., **2016**, *40*, 3933-3949. DOI: 10.1039/C5NJ02608C
38. Jiang, K.; Siahrostami, S.; Zheng, T. T.; Hu, Y. F.; Hwang, S.; Stavitski, E.; Peng, Y.; Dynes, J.; Gangisetty, M.; Su, D., Attenkofer, K. and Wang, H. T. Isolated Ni single atoms in graphene nanosheetsfor high-performance CO_2 reduction. *Energy Environ. Sci*. **2018**, *4*. DOI: 10.1039/C7EE03245E
39. Chen, W.; Pan, X. L. Bao, X. H. Tuning of redox properties of iron and iron oxides via encapsulation within carbon nanotubes. *J. Am. Chem. Soc.* ***2007***, *129*, 7421-7426. DOI: 10.1021/ja0713072
40. Zhang, F.; Jiao, F.; Pan, X.L.; Gao, K.; Xiao, J.P.; Zhang, S.; Bao, X.H. Tailoring the oxidation activity of Pt nanoclusters via encapsulation. *ACS Catal*. **2015**, *5*, 1381-1385. DOI: 10.1021/cs501763k
41. Zhang, C.; Bhargava, G.; Elwell, M. D.; Parasher, S.; Zhou, B.; Yates, D.; Knoke, I.; Neitzel. I.; Gogotsi, Y. Hollow graphitic carbon nanospheres: synthesis and properties. *J. Mater. Sci*. **2014**, *49*, 1947-1956. DOI: 10.1007/s10853-013-7796-5
42. Li, W. H.; Wang, H. Z.; Jiang, X.; Zhu, J.; Liu, Z. M.; Guo, X. W.; Song, C. S. A short review of recent advances in CO_2 hydrogenation to hydrocarbons over heterogeneous catalysts. *RSC Adv*. **2018**, *8*, 7651. DOI: 10.1039/C7RA13546G
43. Weber, D.; He, T.; Wong, M.; Moon, C.; Zhang, A.; Foley, N.; Ramer, N.J.; Zhang, C. Recent Advances in Mitigating Catalyst Deactivation of CO_2 Hydrogenation to Light Olefins. *Catalysts* **2021**, *11*, 1447. DOI: 10.3390/catal11121447
44. Yan, Q.G.; Li, J.H.; Zhang, X.F.; Zhang J.L.; Cai, Z.Y. Mass production of graphene materials from solid carbon sources using a molecular cracking and welding method. *J. Mater. Chem*. A **2019**, *7*, 13978-13985. DOI: 10.1039/C9TA01332F
45. Xiang, W. L.; Zhang, Y. P.; Lin, H. F.; Liu, C. J., Nanoparticle/metal–organic framework composites for catalytic applications: current status and perspective. *Molecules* **2017**, *22*, 2103. DOI: 10.3390/molecules22122103
46. Gupta, S.; Jain, V.K.; Jagadeesan, D., Fine tuning the composition and nanostructure of Fe-based core–shell nanocatalyst for efficient CO_2 hydrogenation. *ChemNanoMat* **2016**, *2*, 989-996. DOI: 10.1002/cnma.201600234
47. Jiang, Q.; Lan, D.P.; Zhao, G.F.; Xu, H.T.; Gong, X.D.; Liu, J.C.; Shi, Y.; Zhang, L.D.; Fang, H.M.; Cheng, D.H.; Ge, J.P.; Xu, Z.L and Liu, J.K. Converting CO_2 Hydrogenation Products from Paraffins to Olefins: Modification of Zeolite surface properties by a UIO-n membrane. *ACS Catal.* **2022**, 12, 5894−5902. DOI: 10.1021/acscatal.2c00785
48. Han,Y.Q.; Xu, H.T.; Su, Y.Q.; Xu, Z.L.; Wang, K.F.; Wang, W.Z. Noble metal (Pt, Au@Pd) nanoparticles supported on metal organic framework (MOF-74) nanoshuttles as high-selectivity CO_2 conversion catalysts, *J. Catal*. **2019**, 370, 70–78. DOI: 10.1016/j.jcat.2018.12.005
49. Tu, J.L.; Ding, M.Y.; Zhang, Q.; Zhang, Y.L.; Wang, C.G.; Wang, T.J.; Ma, L.L.; Li, X.J. Design of carbon-encapsulated Fe_3O_4 nanocatalyst with enhanced performance for Fischer–Tropsch synthesis. *ChemCatChem* **2015**, *7*, 2323–2327. DOI: 10.1002/cctc.201500332

50. Chen, W.; Fan, Z.; Pan, X.; Bao, X.; Chen, W.; Fan, Z.; Pan, X.; Bao, X. Effect of Confinement in carbon nanotubes on the activity of Fischer−Tropsch iron catalyst. *J. Am. Chem. Soc.* **2008**, *130*, 9414 - 9419. DOI: 10.1021/ja8008192
51. Wu, T.; Lin, J.; Cheng, Y.; Tian, J.; Wang, S.; Xie, S.; Pei, Y.; Yan, S.; Qiao, M.; Xu, H.; Zong, B. Porous graphene-confined Fe−K as highly efficient catalyst for CO_2 direct hydrogenation to light olefins. *ACS Appl. Mater. Interfaces* **2018**, *23*, 439-23443. DOI: 10.1021/acsami.8b05411
52. Wei, J.; Sun, J.; Wen, Z.; Fang, C.; Ge, Q.; Xu, H. New insights into the effect of sodium on Fe_3O_4- based nanocatalysts for CO_2 hydrogenation to light olefins. *Catal. Sci. Technol*. **2016**, 6, 4786-4793. DOI: 10.1039/C6CY00160B
53. Wezendonk, T.A.; Sun, X.; Duglan, A.I.; van Hoof, A.J.F.; Hensen, E.J.M.; Kapteijn, F.; Gascon, J. Controlled formation of iron carbides and their performance in Fischer-Tropsch synthesis. *J. Catal*. **2018**, 362, 106−117. DOI: 10.1016/j.jcat.2018.03.034
54. Santos, V.P.; Wezendonk, T.A.; Delgado Jan, J.J.; Dugulan, A.I.; Nasalevich, M.A.; Islam, H.U.; Chojecki, A.; Sartipi, Sun, X.; A. A. Hakeem, A.A.; Koeken, A.C.J.; Ruitenbeek, M.; Davidian, T.; Meima, G.R.; Sankar, G.; Kapteijin F.; Makkee, M.; Gascon, J. Metal organic framework-mediated synthesis of highly active and stable Fischer-Tropsch catalysts. *Nat. Commun*. **2015**, *6*, 6451. DOI: 10.1038/ncomms7451
55. Yu, G.; Sun, B.; Pei, Y.; Xie, S.; Yan, S.; Qiao, M.; Fan, K.; Zhang, X.; Zong, B. Fe(x)O(y)@C spheres as an excellent catalyst for Fischer-Tropsch synthesis. *J. Am. Chem. Soc*. **2010**, *132*, 935 – 937. DOI: 10.1021/ja906370b
56. Zhang, C.; Gao, Q.H.; Parasher, S.; Yates, D. d-Glucose mitigates the agglomeration of the hollow graphitic carbon nanospheres. *J. Mater. Sci*, **2017**, *52* (10): 5968-5980. DOI: 10.1007/s10853-017-0833-z
57. Zhang, C.; Gao, Q.S.; Zhou, B.; Bhargava, G. Preparation, characterization, and surface conductivity of nanocomposites with hollow graphitic carbon nanosphere as fillers in polymethylmethacrylate matrix. *J. Nanopart. Res*. **2017**, *19*, 269. DOI: 10.1007/s11051-017-3976-6
58. Zhang, C.; Fransson, M.; Liu; C. K.; Zhou, B. Carbon nanostructures manufactured from catalytic templating nanoparticles; *US Patent* **2010**. 7,718,155
59. Zhou, B.; Zhang, C.; Balee, R. Polymeric materials incorporating carbon nanosphere nanostructures; *US Patent* **2011**, 7,935276
60. Ravel, B.; Newville, M. ATHENA, ARTEMIS, HEPHAESTUS: data analysis for X-ray absorption spectroscopy using IFEFFIT. *J. Synchrotron Rad*. **2005**, *12*, 537-541 DOI: 10.1107/S0909049505012719
61. Tan, P.H.; Dimovski, S.; Gogotsi, Y. Raman scattering of non-planar graphite: arched edges,polyhedral crystals, whiskers and cones. *Philos. Trans. R. Soc. Lond. A* **2004**, 362, 2289-2310. DOI: 10.1098/rsta.2004.1442
62. Zhang, W.; Shi, X.; Gao, M.; Liu, J.; Lv, Z.; Wang, Y.; Huo, Y.; Cui, C.; Yu, Y.; He, H. Iron-based composite oxide catalysts tuned by CTAB exhibit superior NH_3–SCR performance. *Catalysts* **2021**, *11*, 224. DOI: 10.3390/catal11020224
63. Ye, R.P; Ding, J.; Gong, W.; Argyle, M.D.; Zhong, Q.; Wang, Y.; Russell, C.K.; Xu, Z.; Russell, A.G.; Li, Q.; Fan, M. and Yao, Y.G. CO2 hydrogenation to high-value products via heterogeneous catalysis. Nat. Commun. 2019, 10, 5698. DOI: 10.1038/s41467-019-13638-9
64. Williamson, D.L.; Herdes, C.; Torrente-Murciano, L.; Jones, M.D. and Mattia, D. N-doped Fe@CNT for combined RWGS/FT CO2 Hydrogenation. ACS Sustainable Chem. Eng. 2019, 7, 7, 7395–7402. DOI: 10.1021/acssuschemeng.9b00672

65. Li, Z.Q.; Lu, C.J.; Xia, Z.P.; Zhou, Y.; Luo, Z. X-ray diffraction patterns of graphite and turbostratic carbon. *Carbon* **2007**, 45, 1686-95. Doi: https://doi.org/10.1016/j.carbon.2007.03.038
66. Grosvenor, A.P.; Kobe, B.A.; Biesinger, M.C.; McIntyre, N.S. Investigation of multiplet splitting of Fe 2p XPS spectra and bonding in iron compounds. *Surf. Interface Anal*. **2004**, *36*, 1564–1574. DOI: 10.1002/sia.1984
67. Kuivila, C.S.; Butt, J.B.; Stair, P.C. Compositional aspects of iron Fischer-Tropsch catalysts: an XPS/reaction study. *Appl. Surf. Sci*. **1988**, *32*, 99–121. DOI: 10.1016/0021-9517(89)90319-9
68. Lin, T.C.; Seshadri, G.; Kelber, J.A. A consistent method for quantitative XPS peak analysis of thin oxide films on clean polycrystalline iron surfaces. *Appl. Surf. Sci*. **1997**, *119*, 83–92. DOI: 10.1016/S0169-4332(97)00167-0
69. Slavov, L.; Abrashev, M.V; Merodiiska, T.; Gelev, C.; Vandenberghe, R.E.; Markova-Deneva, I.; Nedkov, I. Raman spectroscopy investigation of magnetite nanoparticles in ferrofluids. *J. Magn. Magn. Mater.* **2010**, 322, 14, 1904-1911. DOI: 10.1016/j.jmmm.2010.01.005
70. Panta, P.C. and Bergmann, C.P. Raman Spectroscopy of Iron Oxide of Nanoparticles (Fe_3O_4). *J. Material Sci. Eng*. **2015**, 5, 1. DOI: 10.4172/2169-0022.1000217
71. Si, H.; Zhou, C.; Wang, H.; Lou, S.; Li, S. Controlled synthesis of different types iron oxides nanocrystals in paraffin oil. *J. Colloid Interface Sci*. **2008**, 327, 466-471. DOI: 10.1016/j.jcis.2008.08.057
72. Zhou, X.; Fang, C.Q.; Li, Y.; An, N.L.; Lei, Q.L. Preparation and characterization of Fe_3O_4-CNTs magnetic nanocomposites for potential application in functional magnetic printing ink, *Compos. B: Eng* **2016**, 89, 295-302. DOI: 10.1016/j.compositesb.2015.11.041
73. Wang, D.; Xie, Z.; Porosoff, M.D.; Chen, J. Recent advances in carbon dioxide hydrogenation to produce olefins and aromatics. *Chem* **2021**, *7*, 1−35. DOI: 10.1016/j.chempr.2021.02.024
74. Zhang, C.; Cao, C.; Zhang, Y.; Liu, X.; Xu, J.; Zhu, M.; Tu, W.; Han, Y. Unraveling the role of zinc on bimetallic Fe_5C_2−ZnO catalysts for highly selective carbon dioxide hydrogenation to high carbon α-olefins. *ACS Catal*. **2021**, *11*, 2121−2133. DOI: 10.1021/acscatal.0c04627

Abstract Graphics

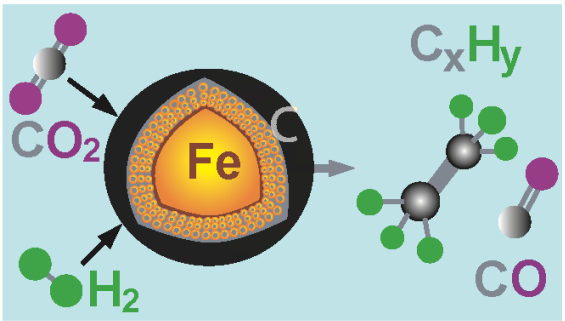

TOC Graphic